JCTC Journal of Chemical Theory and Computation

Article

pubs.acs.org/JCTC

Computation of Dynamic Polarizabilities and van der Waals Coefficients from Path-Integral Monte Carlo

Juha Tiihonen,* Ilkka Kylänpää,† and Tapio T. Rantala

Laboratory of Physics, Tampere University of Technology, P. O. Box 692, FI-33101 Tampere, Finland

ABSTRACT: We demonstrate computation of total dynamic multipole polarizabilities using path-integral Monte Carlo method (PIMC). The PIMC approach enables accurate thermal and nonadiabatic mixing of electronic, rotational, and vibrational degrees of freedom. Therefore, we can study the thermal effects, or lack thereof, in the full multipole spectra of the chosen one- and two-electron systems: H, Ps, He, Ps_2, H_2, and HD^+. We first compute multipole−multipole correlation functions up to octupole order in imaginary time. The real-domain spectral function is then obtained by analytical continuation with the maximum entropy method. In general, sharpness of the active spectra is limited, but the obtained off-resonant polarizabilities are in good agreement with the existing literature. Several weak and strong thermal effects are observed. Furthermore, the polarizabilities of Ps_2 and some higher multipole and higher frequency data have not been published before. In addition, we compute isotropic dispersion coefficients C_6, C_8, and C_{10} between pairs of species using the simplified Casimir−Polder formulas.

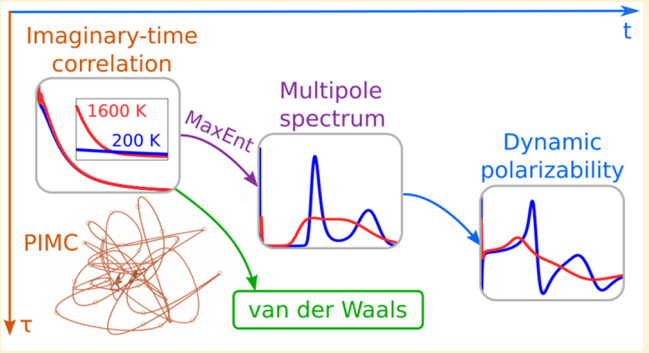

1. INTRODUCTION

Computing dynamic response functions from quantum correlation functions is a popular challenge among quantum Monte Carlo methods, such as path-integral Monte Carlo (PIMC),[1,2] diffusion Monte Carlo (DMC),[3] path-integral molecular dynamics (PIMD),[4,5] and their many derivatives. Purely imaginary-time methods are known to treat quantum many-body correlations very accurately.[6−9] Furthermore, they enable controllable simulation of equilibrium properties, nuclear quantum phenomena, and other nonadiabatic effects—typical banes of the traditional ab initio methods.[10−12] Unfortunately, the strategy of analytic continuation to real-time domain remains a formidable challenge.

A quantum correlation function of a causal process is analytic in the complex plane,[13] and thus, it can be transformed between purely imaginary and real axes by Kubo transform.[14] Unfortunately, numerical implementation of such an inversion is an infamous ill-posed problem: even small noise in the imaginary-time data maps large fluctuations onto the real-time response. Different strategies have been developed to get around this problem: complex time propagators,[15,16] Pade approximants,[17] SVD sampling[18] and Mishchenko's method.[19,20] None of the approaches is superior, yet one of the most popular approaches is maximum entropy (MaxEnt),[21,22] which optimizes the balance between prior information and a least-squares fit. It will be used in this work, too.

Fortunately, the same means of solution can be applied to a wide variety of physical problems. For dedicated reviews, see refs 1, 5, and 23. Quantum correlation functions and analytic continuation have been employed in the computation of, e.g., magnetic susceptibility,[24] density of states,[18] NMR relaxation rate,[25] absorption spectra and transport properties,[26,27] polarons,[19] and optical conductivity.[28]

In this work, we focus on the electric field response: dynamic multipole polarizability. Polarizability is, arguably, the most important of all electronic properties. It is an important parameter in nonlinear optics, spectroscopy, and a wide variety of other physical experiments.[29] Furthermore, it is gaining popularity in molecular interaction models and polarizable force fields.[30,31] Most importantly, the accurate computation of polarizability is a theoretical challenge and a powerful benchmark for any electronic structure methods.[32−38]

Our purpose is to demonstrate the computation of dynamic polarizabilities from PIMC simulations. Similar approaches in imaginary time have been exercised before for static polarizabilities,[39−43] but, to the best of our knowledge, this work is the first one featuring real-time response of the given problem. Explicit all-electron simulation is not the most typical application of the PIMC method, because of its computational cost. However, it provides some obvious benefits over the traditional ab initio methods, such as inherent accounts of finite temperature and exact many-body correlations. Besides the electronic structure, PIMC also enables fully nonadiabatic and quantum mechanical treatment of the nuclear degrees of freedom: rotation and vibration. All of these have different thermal effects on polarizability.[42,44,45] Especially, the infrared (IR)-active species have huge thermal effects on rotational polarizabilities,[46,47] which are also closely associated with IR and Raman spectroscopy.[48,49]

Received: August 23, 2018
Published: October 2, 2018

DOI: 10.1021/acs.jctc.8b00859
J. Chem. Theory Comput. XXXX, XXX, XXX−XXX

We provide exemplary results, i.e., dynamic polarizabilities and dispersion coefficients up to octupole order, for several isolated atoms and molecules: H, He, HD^+, H_2, Ps, and Ps_2. The chosen species feature accurate reference data for validation[47,50−55] but also some exotic properties that have barely been studied before. In particular, we are able to reproduce known electronic polarizabilities at low frequencies and provide an estimate for the rest of the whole power spectrum, where no prior reference data exist. All the electronic, nuclear, and nonadiabatic effects are included in these total polarizabilities. Especially, we can easily quantify the dielectric properties of an ultimately nonadiabatic problem, Ps_2. Finally, we provide dispersion coefficients C_6, C_8, and C_{10} between pairs of the considered species.

The work is organized as follows. First, we review the theoretical background by using linear response theory and properties of Green's functions. We associate first-order dynamic polarizabilities with spectral functions, which are obtained from electric multipole correlation functions by a nonlinear inversion. In section 3, we review the practical aspects of computing the imaginary-time correlation functions with PIMC and performing the numerical inversion with MaxEnt. Finally, we present and discuss the results with suitable literature references.

2. THEORY

We consider a quantum system in an external optical perturbation, that is, a classical electric field $\mathbf{F}(t)$. The total Hamiltonian can be written as

$$\hat{H}(t) = \hat{H}_0 + \hat{H}_{\text{ext}}(t) \tag{1}$$

where $\hat{H}_0$ is a time-independent part

$$\hat{H}_0 = \hat{T} + \sum_{i>j} \hat{V}_{ij}(r) \tag{2}$$

where $\hat{T}$ and $\hat{V}_{ij}(r)$ are operators for kinetic energy and Coulomb interaction energy, respectively. The time-dependent perturbation is

$$\hat{H}_{\text{ext}}(t) = -\theta(t - t')\, \mathbf{F}(t)\cdot\hat{\mathbf{Q}} \tag{3}$$

where the Heaviside step function $\theta(t-t')$ denotes switching on the perturbation at time t'. The interaction $\hat{\mathbf{Q}}$ with the vector field $\mathbf{F}$ can be decomposed in the multipole expansion as[56]

$$\mathbf{F}\cdot\hat{\mathbf{Q}} = -\sum_{n=0}^{\infty} \frac{2^n n!}{(2n)!} F^{(n)}[n]\hat{Q}^{(n)} \tag{4}$$

where we have the net charge $F^{(0)} = q$ in electrostatic potential $\hat{Q}^{(0)} = \phi$. The electric multipole moments (dipole, quadrupole, and octupole, etc.)

$$\hat{Q}^{(1)} = \hat{\mu}, \quad \hat{Q}^{(2)} = \hat{\mathbf{\Theta}}, \quad \hat{Q}^{(3)} = \hat{\mathbf{\Omega}}, \quad \text{etc.} \tag{5}$$

and field gradients

$$F^{(1)} = \mathbf{F}, \quad F^{(2)} = \nabla\mathbf{F}, \quad F^{(3)} = \nabla\nabla\mathbf{F}, \quad \text{etc.} \tag{6}$$

are typically defined according to the center of mass. The n-dot product $[n]$ consists of the summation of corresponding tensorial components to produce a scalar potential, e.g., $Q^{(2)}[2]F^{(2)} = \sum_{i,j}\nabla\Theta_{ij}(\nabla F)_{ij}$. Thus, the perturbation up to the third order is written as

$$\hat{H}_{\text{ext}}(t) = -\theta(t - t') \times \left[\hat{\mu}\cdot\mathbf{F}(t) + \frac{1}{3}\hat{\mathbf{\Theta}}\!:\!(\nabla\mathbf{F}(t)) + \frac{1}{15}\hat{\mathbf{\Omega}}\!:\!(\nabla\nabla\mathbf{F}(t))\right] \tag{7}$$

In the following treatment of spherically symmetric systems, we will omit the tensorial character and only consider scalar electric moments and field gradients.

2.1. Linear Response Theory. In many-body quantum mechanics, the linear response of some property P can be summarized as follows. $\hat{Q}$ denotes any of the perturbing operators in eq 5 and $F(t)$ a corresponding field term. In a causal scenario, the perturbation starts at time t' and the response is measured at time $t > t'$. The linear deviation can be written as

$$\delta P(t) = \frac{i}{\hbar}\int_{-\infty}^{t} \mathrm{d}t'\, \langle[\hat{H}_{ext}(t'), \hat{P}(t)]\rangle \tag{8}$$

$$= \frac{i}{\hbar}\int_{-\infty}^{t} \mathrm{d}t'\, \theta(t - t')\langle[\hat{P}(t - t'), \hat{Q}(0)]\rangle F(t') \tag{9}$$

$$= \int_{-\infty}^{\infty} \mathrm{d}t'\, \chi^R(t - t')\, F(t') \tag{10}$$

where square brackets denote a commutator and angle brackets a thermal average, $\langle\hat{A}\rangle \equiv \mathrm{Tr}[\hat{\rho}\hat{A}]/\mathrm{Tr}[\hat{\rho}]$, where $\hat{\rho} = \mathrm{e}^{-\beta\hat{H}}{}_0$ and $\beta = 1/k_B T$. On the second line we have used the time invariance of thermal equilibrium, and on the third line we have inserted the retarded susceptibility

$$\chi^R(t) = \frac{i}{\hbar}\theta(t)\langle[\hat{P}(t), \hat{Q}(0)]\rangle = -G^R(t) \tag{11}$$

where G^R is the retarded Green's function of $\hat{P}$ and $\hat{Q}$ and the negative sign follows from the usual convention of electric field perturbation. Frequency-dependent response is given by the Fourier transform

$$\delta P(\omega) = \mathcal{F}\delta P(t) = \chi^R(\omega)\, F(\omega) \tag{12}$$

based on the convolution theorem in eq 10. We can without loss of generality treat eq 12 in terms of a single frequency ω, because arbitrary signals and responses can be superposed from the harmonic waves.[57]

The subject of interest is the constant of proportionality, the complex susceptibility $\chi^R(\omega)$. It is also analytic in the upper complex plane, and thus, it can be expressed with the Kramers−Kronig relations as[21]

$$\chi^R(\omega) = -\int_{-\infty}^{\infty} \frac{\mathrm{d}\omega'}{\pi}\frac{\mathrm{Im}[\chi^R(\omega')]}{\omega - \omega' + i\eta} \tag{13}$$

where η is a positive infinitesimal. For reasons that will become apparent, we shall write it in terms of a spectral function $A(\omega)$:

$$\chi^R(\omega) = -\int_{-\infty}^{\infty} \frac{\mathrm{d}\omega'}{2\pi}\frac{A(\omega')}{\omega - \omega' + i\eta} \tag{14}$$

where we defined[58]

$$A(\omega) = i[G^R(\omega) - [G^R(\omega)]^\dagger] = -2\mathrm{Im}[G^R(\omega)] = 2\mathrm{Im}[\chi^R(\omega)] \tag{15}$$

where the advanced Green's function $[G^R]^\dagger$ is the Hermitian conjugate of G^R. The spectral function $A(\omega)$ has real and positive-semidefinite values, which are related to transition probabilities. Outside the spectral region, i.e., when $A(\omega) \sim 0$, $\chi^R(\omega)$ is effectively real and equal to the dielectric response of

DOI: 10.1021/acs.jctc.8b00859
J. Chem. Theory Comput. XXXX, XXX, XXX−XXX

the system, i.e., polarizability. Within a spectral peak, $\chi^R(\omega)$ becomes complex, and the imaginary part is related to the absorption/emission probability.

2.2. Imaginary-Time Correlation. Most quantum Monte Carlo methods operate in imaginary time: $-it \rightarrow \tau$, because imaginary-time propagators are well-behaved and the acquisition of correlation functions along an imaginary-time trajectory is straightforward. The imaginary-time Green's functions are defined as

$$\mathcal{G}(\tau) = \langle \mathcal{T}_\tau \hat{P}(0)\, \hat{Q}(\tau)\rangle \tag{16}$$

where $\mathcal{T}_\tau$ is a time-ordering operator in the imaginary axis. Equation 16 is the equivalent of $\chi^R(t)$ with a purely imaginary argument. At finite temperature, the Green's function is periodic over the inverse temperature β. That is, $0 \le \tau \le \beta$ and eq 16 satisfy $\mathcal{G}(\tau) = \pm\mathcal{G}(\tau + \beta)$, where the positive (negative) sign is for bosons (fermions). The Fourier transform is given in discrete Matsubara frequencies ω_n:

$$\mathcal{G}(i\omega_n) = \int_0^\beta \mathrm{d}\tau\ \mathrm{e}^{-i\omega_n\tau}\, \mathcal{G}(\tau) \tag{17}$$

which are $(2n + 1)\pi/\beta$ for fermions and $2n\pi/\beta$ for bosons.

As before, $\mathcal{G}$ is analytic in the upper complex plane and can be represented with the spectral function:[21,22]

$$\mathcal{G}(\tau) = \int_{-\infty}^{\infty} \frac{\mathrm{d}\omega}{2\pi}\, K(\tau, \omega)\, A(\omega) \tag{18}$$

$$\mathcal{G}(i\omega_n) = \int_{-\infty}^{\infty} \frac{\mathrm{d}\omega}{2\pi}\, K(i\omega_n, \omega)\, A(\omega) \tag{19}$$

where the respective kernels for time and frequency domains are $K(\tau,\omega) = \mathrm{e}^{-\tau\beta}/(1 \pm \mathrm{e}^{-\beta\omega})$ (plus for bosons, minus for fermions) and $K(i\omega_n,\omega) = 1/(i\omega_n - \omega)$. That is, imaginary-time Green's functions can be analytically continued to the real domain by inverting eq 18 or 19. For that, the spectral function is a good agent, because it is (usually) positive-semidefinite and regularized. However, as both kernels are highly nonlinear, numerical inversion is challenging, to say the least.

2.3. Multipole Polarizability. Dynamic multipole polarizability α is by definition the linear response of an electric moment P to a perturbation F that couples to Q, i.e., $\alpha(\omega) = \chi^R(\omega)$. In particular, one can calculate the Fourier transform of eq 9 for a harmonic perturbation $F(t') = \mathrm{e}^{i\omega t'}F$:

$$\begin{aligned}\delta P(\omega) &= \frac{i}{\hbar}\int_{-\infty}^{\infty} \mathrm{d}t\ \mathrm{e}^{-i\omega t} \\ &\quad \times \int_{-\infty}^{t} \mathrm{d}t'\theta(t - t')\langle[\hat{P}(t - t'), \hat{Q}(0)]\rangle \mathrm{e}^{i\omega t'}F \\ &= \frac{i}{\hbar}\int_0^{\infty} \mathrm{d}(t - t')\ \mathrm{e}^{-i\omega(t-t')}\langle[\hat{P}(t - t'), \hat{Q}(0)]\rangle F\end{aligned} \tag{20}$$

where F is an amplitude. The integral can be calculated, when the correlation function is expanded in the energy eigenstates:

$$\begin{aligned}&\langle[\hat{P}(t - t'), \hat{Q}(0)]\rangle \\ &= \sum_n^{\infty} \frac{\mathrm{e}^{-\beta E_n}}{Z} \sum_m^{\infty} (P_{nm}Q_{mn}\mathrm{e}^{-i\omega_{mn}(t-t')} - Q_{mn}P_{nm}\mathrm{e}^{+i\omega_{mn}(t-t')})\end{aligned} \tag{21}$$

where $\omega_{mn} = (E_m - E_n)/\hbar$ and, e.g., $Q_{mn} = \langle m|\hat{Q}|n\rangle$. Assuming that $F(t') \rightarrow 0$ as $t - t' \rightarrow \infty$, one can then identify the susceptibility as

$$\chi^R(\omega) = \sum_n^{\infty} \frac{\mathrm{e}^{-\beta E_n}}{\hbar Z} \sum_m^{\infty} \left[\frac{P_{mn}Q_{mn}}{\omega_{mn} - \omega} + \frac{Q_{mn}P_{nm}}{\omega_{mn} + \omega}\right] \tag{22}$$

$$\equiv \langle\alpha^-(\omega)\rangle + \langle\alpha^+(\omega)\rangle \tag{23}$$

$$\equiv \langle\alpha(\omega)\rangle \tag{24}$$

where $\alpha^-(\omega)$ and $\alpha^+(\omega)$ are the so-called resonant and antiresonant polarizabilities. In the zero Kelvin limit, i.e., $\beta \rightarrow \infty$, one recovers the usual sum-overstates definition of polarizability from eq 23.

In this work, we will consider isotropic polarizabilities, such as those of gaseous atoms and molecules. Consequently, all polarizabilities with an "odd" degree, such as $\chi^R_{\mu\Theta}$, cancel out in spherical averaging. We will thus consider the following even first-order properties (but omit $\chi^R_{\mu\Omega}$ for simplicity)

$$\alpha_1 \equiv \chi^R_{\mu\mu} \quad \text{(dipole−dipole)} \tag{25}$$

$$\alpha_2 \equiv \chi^R_{\Theta\Theta} \quad \text{(quadrupole−quadrupole)} \tag{26}$$

$$\alpha_3 \equiv \chi^R_{\Omega\Omega} \quad \text{(octupole−octupole)} \tag{27}$$

where P and Q are in turn replaced by μ, Θ, and Ω. These are scalar polarizabilities, meaning that the tensorial character is also lost in isotropic sampling.

Alternatively, one could compute polarizability in the internal coordinates of a molecule and find anisotropy, which leads to a tensorial response. While it goes against the measurable realm, moving to internal coordinates has some virtues: the first-order anisotropy adds insight into the optical response of the molecule, and it also reflects strongly to the rotational higher-order perturbations, the hyperpolarizabilities.[41−43,46] Often, only tensorial electronic polarizabilities have been reported, which omit the nuclear effects or treat them separately. In that case, isotropic averaging is required to make such results comparable with those in the "laboratory coordinates". For diatomic molecules, it is given in the first two degrees by[46,59]

$$\langle\alpha_1\rangle = (2\alpha_{xx} + \alpha_{zz})/3 \tag{28}$$

$$\langle\alpha_2\rangle = (\alpha_{zz,zz} + 8\alpha_{zx,zx} + 8\alpha_{xx,xx})/15 \tag{29}$$

where z is the principal axis.

2.4. Dispersion Coefficients. Lastly, we use polarizabilities in the computation of van der Waals, or more precisely, London dispersion coefficients. The coefficients are used to model attractive interactions between atoms and molecules due to quantum fluctuations of electric moments. After spherical averaging, the radial pair interaction between species A and B is quantified as

$$V^{AB}(r) = -\frac{C_6^{AB}}{r^6} - \frac{C_8^{AB}}{r^8} - \frac{C_{10}^{AB}}{r^{10}} - \cdots \tag{30}$$

where C_6, C_8, and C_{10} are the dispersion coefficients. Accurate calculation of the higher-order terms C_8 and C_{10} can be especially challenging, while their effect can be considerable.[60] According to the simplified Casimir−Polder formulas, the coefficients are defined in terms of dynamic polarizabilities with imaginary-frequency argument:[50]

DOI: 10.1021/acs.jctc.8b00859
J. Chem. Theory Comput. XXXX, XXX, XXX−XXX

$$C_6^{AB} = \frac{3}{\pi}\int_0^\infty \mathrm{d}\omega\ \alpha_1^A(i\omega)\,\alpha_1^B(i\omega) \tag{31}$$

$$C_8^{AB} = \frac{15}{2\pi}\int_0^\infty \mathrm{d}\omega\ (\alpha_1^A(i\omega)\,\alpha_2^B(i\omega) + \alpha_2^A(i\omega)\,\alpha_1^B(i\omega)) \tag{32}$$

$$C_{10}^{AB} = \frac{14}{\pi}\int_0^\infty \mathrm{d}\omega\ (\alpha_1^A(i\omega)\,\alpha_3^B(i\omega) + \alpha_3^A(i\omega)\,\alpha_1^B(i\omega)) + \frac{35}{\pi}\int_0^\infty \mathrm{d}\omega\ \alpha_2^A(i\omega)\ \alpha_2^B(i\omega) \tag{33}$$

Based on eq 17, the required polarizabilities are obtained from the imaginary-time correlation functions at discrete Matsubara frequencies by a regular Fourier transform. The continuous integral can be evaluated with good accuracy by interpolating the smooth Matsubara data.

3. METHOD

The workflow of this study can be summarized in five steps:

1. PIMC computation of imaginary-time correlation function $\mathcal{G}(\tau)$;
2. Fourier transform to imaginary Matsubara frequencies $\mathcal{G}(i\omega_n)$;
3. MaxEnt inversion of eq 19 to obtain $A(\omega)$;
4. transformation with eq 14 to obtain dynamic polarizability $\alpha(\omega)$;
5. calculation of dispersion coefficients from $\alpha(i\omega_n)$.

We will provide an overview and some practical details in the following subsections.

3.1. Path-Integral Monte Carlo. To compute imaginary-time correlation functions $\mathcal{G}(\tau)$, we use a private implementation of the standard path-integral Monte Carlo method (PIMC).[1,2,61] Depending on the nature of the problem, other methods could be used as well; e.g., see refs 5 and 39. Measuring the correlation function itself is straightforward; the important factors are the accuracy and efficiency of the simulation. All-electron simulation of atomic species is not yet common with the PIMC method, because of its computational cost. However, it is needed to properly extract electronic properties, such as polarizabilities, in combination with the nuclear quantum effects: rotation, vibration, and, in principle, nonadiabatic coupling.

In thermal equilibrium defined by $\beta = 1/kT$, expectation values are given by

$$\langle O\rangle = Z^{-1}\mathrm{Tr}[\hat{\rho}(\beta)\hat{O}] \tag{34}$$

where $Z = \mathrm{Tr}\hat{\rho}(\beta)$ and $\hat{\rho}(\beta) = \mathrm{e}^{-\beta\hat{H}}$. The essence of PIMC is expansion of the density matrix $\rho(\beta)$ into a discrete imaginary-time path

$$\begin{aligned}\rho(R, R; \beta) &= \int \mathrm{d}R\ \langle R|\hat{\rho}(\beta)|R\rangle \\ &= \int \mathrm{d}R\ \langle R|\hat{\rho}(\Delta\tau)^M|R\rangle \\ &= \int \mathrm{d}R_1 \ldots dR_M\ \langle R_0|\hat{\rho}(\Delta\tau)|R_1\rangle\ldots\langle R_{M-1}|\hat{\rho}(\Delta\tau)|R_M\rangle\end{aligned} \tag{35}$$

where R is a position representation of the many-body state, $M = \beta/\Delta\tau \gg 1$ is the Trotter number, and $R = R_M = R_0$ closes the ring polymer. Accuracy of the propagator $\mathrm{e}^{-\Delta\tau\hat{H}}$ can be controlled by adjusting the short time step $\Delta\tau$. In this work, we use exact pair-density matrices that are obtained from the Coulomb potential by matrix squaring,[61,62] and $\Delta\tau$ dictates the validity of the pair approximation.

In particular, a correlation function between $\hat{P}$ and $\hat{Q}$ is given by

$$\begin{aligned}\langle\mathcal{G}(m\Delta\tau)\rangle &= \langle\mathcal{T}_\tau P(0)\ Q(\tau)\rangle \\ &= Z^{-1}\int \mathrm{d}R_1 \ldots \mathrm{d}R_M \\ &\quad\times \langle R_0|\hat{\rho}(\Delta\tau)|R_1\rangle\ldots\langle R_{M-1}|\hat{\rho}(\Delta\tau)|R_M\rangle P(R_0)\ Q(R_m)\end{aligned} \tag{36}$$

$$\begin{aligned}&= Z^{-1}M^{-1}\sum_{k=0}^{M-1}\int \mathrm{d}R_1 \ldots \mathrm{d}R_M \\ &\quad\times \langle R_0|\hat{\rho}(\Delta\tau)|R_1\rangle\ldots\langle R_{M-1}|\hat{\rho}(\Delta\tau)|R_M\rangle P(R_k)\ Q(R_{m+k})\end{aligned} \tag{37}$$

where $0 \le m$ and $m + k \le M - 1$ are periodic in M and $O(R_m)$ denotes a measurement at a particular time slice. Equation 37 also utilizes symmetry of the equilibrium so that the average correlation can be measured with respect to any, or every, time slice. In practice, careless computation of all $M \times M$ correlations can be very costly in terms of both performance and data storage. A lot of efficiency can be recovered by utilizing the symmetry properties and optimizing loops and memory usage of the implementation. More details and an optimized pseudocode are provided in Appendix A.

Another computationally intensive part is sampling the integral $\int \mathrm{d}R$ over all possible paths. In PIMC, the many-body trajectory R is a Markovian walker that is sampled in thermal equilibrium using the Metropolis algorithm. Sampling efficiency is a result of many factors, such as the temperature, density, number of particles, fermion/boson statistics, and the finite time step $\Delta\tau$. In this work, we use the bisection method[2] in combination with random rotations. Also, for now we only simulate systems with distinguishable particles that can be solved exactly using the so-called boltzmannon statistics. By choosing to exclude identical fermions, we avoid having to treat self-canceling permutations that lead to degradation of efficiency due to the infamous sign problem.[63]

3.2. Fourier Transforming $\mathcal{G}(\tau)$. When a satisfactory estimate of $\langle\mathcal{G}(\tau)\rangle$ has been produced, it is time for postprocessing. The first follow-up step is Fourier transforming $\mathcal{G}(\tau)$ to give $\mathcal{G}(i\omega_n)$ in terms of discrete Matsubara frequencies ω_n. The alternative would be using eq 18 for the MaxEnt inversion, but the frequency kernel $K(i\omega_n,\omega)$ is considered better behaving.[22] The Matsubara data are also equated with the polarizability; i.e., $\mathcal{G}(i\omega_n) = \alpha(i\omega_n)$, which will be used in eqs 31−33).

The Fourier transform can be performed discretely; i.e.,

$$\mathcal{G}(i\omega_n) = \int_0^\beta \mathrm{d}\tau\ \mathrm{e}^{i\omega_n\tau}\,\mathcal{G}(\tau) \tag{38}$$

$$= \lim_{M\to\infty}\sum_{m=0}^{M-1}\Delta\tau\mathrm{e}^{i\omega_n m\Delta\tau/M}\,\mathcal{G}(m\Delta\tau) \tag{39}$$

where $\Delta\tau = \beta/M$ defines the sampling resolution. Practically, $\Delta\tau$ needs not to be zero, but a small finite value provides enough accuracy for a reasonable number of Matsubara frequencies. A typical process is visualized in Figure 1: fast Fourier transform (FFT) maps M original MC values of $\langle\mathcal{G}(m\tau)\rangle$ into equally many Matsubara frequencies. Beyond a fraction of the frequencies, there will be an error, unless $\Delta\tau$ is artificially decreased by some integer factor, e.g., 8. This consists of numerical interpolation of the data, which can be done for example with cubic splines. Alternatively, the spline-interpolated data can be Fourier transformed analytically,[22] but the practical difference is negligible. Furthermore, due to the

DOI: 10.1021/acs.jctc.8b00859
J. Chem. Theory Comput. XXXX, XXX, XXX−XXX

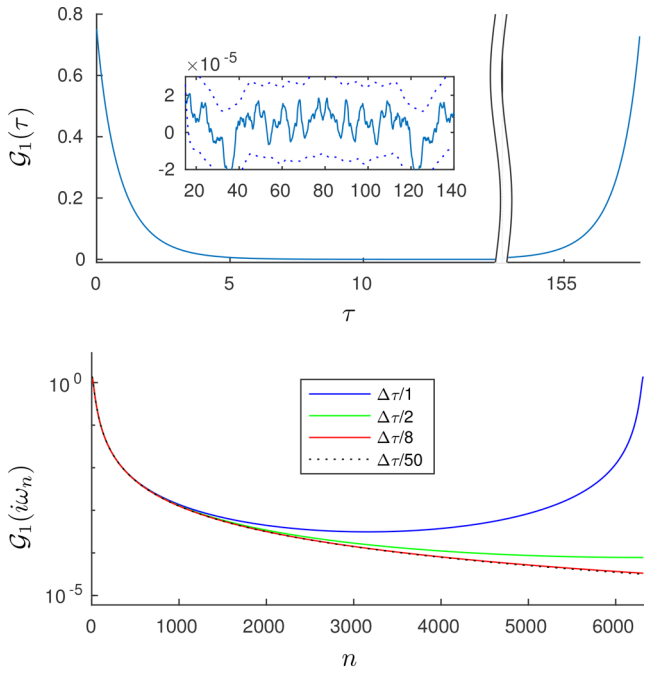

Figure 1. Top, total $\mathcal{G}_1(\tau)$ of He at 2000 K. Noisy fluctuation near $\langle\mu\rangle^2 = 0$ is depicted in the inset. Bottom, same data given in discrete Matsubara frequencies, $\alpha_1(i\omega_n)$. Discrete Fourier transform wrongfully produces periodic data. One way to approach the true Matsubara data is to increase the period by adjusting the relative interpolation density from $1/\Delta\tau$ to infinity. Since the absolute magnitude of $\alpha_l(i\omega_n)$ drops fast, and only a fraction of Matsubara frequencies contribute to $\alpha_l(\omega)$ or dispersion coefficients, we have chosen $\Delta\tau/8$ as a safe interpolation frequency.

linearity of Fourier transform, it does not matter, whether we transform the sample average or average over transforms of samples; i.e.,

$$\langle\mathcal{G}(i\omega_n)\rangle = \mathcal{F}\langle\mathcal{G}(\tau)\rangle = \langle\mathcal{F}\mathcal{G}(\tau)\rangle \tag{40}$$

We prefer the right-hand side (rhs) of eq 40, because it provides a tangible interface to the statistics of $\langle\mathcal{G}(i\omega_n)\rangle$.

In conclusion, using FFT with the original $\Delta\tau$ is tempting but only realiable for the lowest fraction of Matsubara frequencies. This can be resolved by boosting the sampling resolution of $\mathcal{G}(\tau)$ and, thus, reaching even higher frequencies. On the other hand, FFT is exact at the static limit, i.e., $\alpha(i\omega_n{=}\omega{=}0)$. There we have, for instance

$$\begin{aligned}\alpha_1(0) &= \sum_{m=0}^{M-1} \Delta\tau e^{i\omega_n m\Delta\tau/M}\langle\mathcal{G}_1(m\Delta\tau)\rangle \\ &= \sum_{m=0}^{M-1}\Delta\tau\left\langle M^{-1}\sum_{k=0}^{M-1}\mu(R_k)\,\mu(R_{k+m})\right\rangle \\ &= M\Delta\tau\left\langle M^{-2}\sum_{m=0}^{M-1}\mu(R_m)\sum_{k=0}^{M-1}\mu(R_k)\right\rangle \\ &= \beta\langle\bar{\mu}^2\rangle\end{aligned}$$

where bar denotes an average over a sample path. The last form eclipses the static field-derivative estimators that have been proposed earlier.[42,43] The relative number of independent measurements needed by these static estimators is reduced from M^{d+1} to $(d+1)M$, where d is the degree of polarizability, here 1.

3.3. Maximum Entropy Method. Solving integral eq 18 or 19 is challenging, when $\mathcal{G}$ on the left-hand side is noisy or incomplete. While quantum Monte Carlo results can be, in principle, improved indefinitely, the statistical noise cannot be fully eliminated. Thus, even minor fluctuations in the high values of τ or ω can reflect strongly in the resulting spectral function $A(\omega)$. Normally, one could discretize τ or ω and solve the resulting linear system

$$\mathbf{G} = \mathbf{K}\mathbf{A} \tag{41}$$

where $\mathbf{G}$ and $\mathbf{A}$ are discrete input and output vectors, respectively, and $\mathbf{K}$ is a transformation matrix to be inverted. Unfortunately, here the kernel producing $\mathbf{K}$ is highly nonlinear. We could end up with very diverse results just by using different grids or MC samples.

Therefore, a robust method is needed for the inversion, and one of the most popular is maximum entropy (MaxEnt).[21,22] MaxEnt uses Bayesian inference to pick the most probable $\mathbf{A}$ out of all possible solutions with a given $\mathbf{G}$. This is equal to maximizing

$$P(\mathbf{A}|\mathbf{G}) = \frac{P(\mathbf{G}|\mathbf{A})\,P(\mathbf{A})}{P(\mathbf{G})} \tag{42}$$

First, $P(\mathbf{G})$ can be considered fixed. Second, the relative probability of $\mathbf{G}$ given $\mathbf{A}$ can be quantified by the central limit theorem as

$$P(\mathbf{G}|\mathbf{A}) \propto e^{-\chi^2/2} \tag{43}$$

where

$$\chi^2 = (\mathbf{G}-\bar{\mathbf{G}})^{\mathrm{T}}\mathbf{C}^{-1}(\mathbf{G}-\bar{\mathbf{G}}) \tag{44}$$

where $\bar{\mathbf{G}} = \mathbf{K}\mathbf{A}$ is the proposed forward mapping and $\mathbf{C}$ is the covariance matrix. In other words, χ^2 is a least-squares fitting error between the input and the proposed mapping. Lastly, the prior probability can be defined as

$$P(\mathbf{A}) \propto e^{aS} \tag{45}$$

where

$$S = -\int\frac{d\omega}{2\pi}A(\omega)\ln\left(\frac{A(\omega)}{D(\omega)}\right) \tag{46}$$

is called the relative entropy. $D(\omega)$ is the so-called default model that sets an a priori bias for the entropy. It can be used to steer the fitting by setting it to resemble the expected shape of the spectral function.

Combining eqs 43 and 45, the inversion boils down to maximizing

$$\ln P(A|G) = aS - \chi^2/2 \tag{47}$$

for a given frequency grid and a. Again, a is an adjustable parameter that balances the fit between the least-squares error and the default model: too small a favors overfitting to statistical noise, while too large a returns the default model and shuns any new information. There are several strategies for identifying the optimal a, e.g., classical, historic, and the Bryan's approach. It is indeed one of the most important practical choices, along with specifying the ω-grid and the default model $D(\omega)$.

DOI: 10.1021/acs.jctc.8b00859
J. Chem. Theory Comput. XXXX, XXX, XXX−XXX

In this work, we use OmegaMaxEnt software (ΩMaxEnt, version 2018-01) by Bergeron and Tremblay.[22] It uses fitted spectral moments to regulate the output and maximum curvature of the $\log(\chi^2)-\log(a)$ plot to identify the optimal a. It is thus relatively independent of the choice of $D(\omega)$, which makes for a good black box. For further details on the implementation and techniques, we refer to ref 22 and the user documentation.

A few practical notes on the use of ΩMaxEnt are in order. First, for first-order polarizabilities we choose a *bosonic calculation*, which enforces the problem to positive frequencies, only. For the input, we use a real-valued $\mathcal{G}(i\omega_n \geq 0)$ and its *real covariance matrix* $\mathbf{C}$, which are estimated from a set of Fourier transformed PIMC results. In practice, the input data must be truncated to $n_{\max}$ lowest Matsubara frequencies based on a few rules of thumb: there has to be many enough high frequencies to converge the estimation of spectral moments; yet, for too large $n_{\max}$, the inputs become unreliable due to random noise. A particular problem is the covariance matrix $\mathbf{C}$, which will be inverted and needs to be nonsingular. However, by increasing the number of MC samples, we get a more accurate estimate of $\mathbf{C}$, and enable more Matsubara frequencies to be used. In this work, the number is usually between 50 and 800.

A *non-uniform grid in main spectral range* is manually adjusted to promote resolution in the active spectral regions: the electronic peaks and, with some molecules, the low-frequency rotational spectra. We choose not to modify $D(\omega)$ from the software default, which is a normalized Gaussian function centered at $\omega = 0$, whose variance depends on the estimated spectral moments. Finally, the output data are given in the form $\frac{1}{2}A(\omega)/\omega$, where the negative frequencies obey antisymmetry $A(\omega) = -A(-\omega)$. Unfortunately, we cannot reliably estimate the error of $A(\omega)$, but the typical qualitative error is that collections of sharp peaks are replaced by a single soft form. This is exemplified in Figure 2, which also demonstrates one of the integral properties of MaxEnt: while increasingly tedious, providing better input improves the result by sharpening the spectrum while roughly maintaining its original weight.

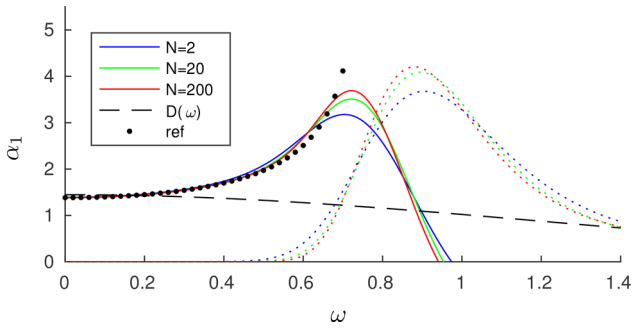

Figure 2. Improvement of the MaxEnt spectrum of He at 2000 K as a function of input data quality. The real (solid) and imaginary (dotted) components of the dynamic polarizability $\alpha_1(\omega)$ are plotted using a variable number of data blocks N, an arbitrary measure of computational effort. Even low-quality data produce a qualitatively meaningful spectrum. The off-resonant data are good, but near the active spectral region the MaxEnt data divert from the 0 K reference.[50] Providing better input data improves the sharpness systematically. However, using this means to achieve narrow peaks with purely physical spectral broadening leads to ill-conditioned scaling of computation. A better strategy would be improving the default model $D(\omega)$ (dashed), which is rather plain in this work.

3.4. Integral Transforms. The last two steps only involve integral transforms of discrete numerical data. For both, the actual integration is done numerically using the trapezoidal rule with dense cubic spline interpolation.

The first transform, eq 14, can be rewritten as

$$\alpha(\omega) = -\int_{-\infty}^{\infty} \frac{d\omega'}{2\pi} \frac{A(\omega')}{\omega - \omega' + i\eta} = \int_0^{\infty} \frac{d\omega'}{2\pi} A(\omega') \left[\frac{1}{\omega' - \omega - i\eta} + \frac{1}{\omega + \omega' + i\eta} \right] \quad (48)$$

which is convenient, because the input is given as $A(\omega \geq 0)$. It also represents the resonant and antiresonant terms of polarizability. Practically, the integration can be truncated after the main spectral region, at around $\hbar\omega' \sim 10$ at maximum. Setting the dissipation term to $\eta = 0.001$ appears to produce convergent results.

The calculation of dispersion coefficients involves products of polarizabilities for two species (or just one paired with itself). Thus, the integrand is nonlinear in the MC data, which has a few consequences: First, random fluctuations in $\langle \alpha(i\omega_n) \rangle$ may not exactly cancel out. This cannot be eliminated completely, but some of the noise can be filtered out by smoothing the data before integration with the moving average technique. Second, the error estimate for each integrated term ΔC_* is written as

$$(\Delta C_*)^2 = \int_0^{\infty} d\omega \, (\alpha_{l_1}^A(i\omega) \, \Delta\alpha_{l_2}^B(i\omega))^2 + (\Delta\alpha_{l_1}^A(i\omega) \, \alpha_{l_2}^B(i\omega))^2 + \alpha_{l_1}^A(i\omega) \, \alpha_{l_2}^B(i\omega) \, \Delta\alpha_{l_1}^A(i\omega) \, \Delta\alpha_{l_2}^B(i\omega) \quad (49)$$

where l_1 and l_2 take values of 1, 2, and 3, and the integral is in practice replaced by a sum over the components of $\Delta\omega$. As before, $\langle \alpha(i\omega_n) \rangle$ decays fast in the growing n, and thus, the integration can be safely truncated at, e.g., $n = M$.

4. RESULTS

We estimate dynamic polarizability for a collection of systems with one or two electrons: H, He, Ps, Ps_2, HD^+, and H_2. The list is not exhaustive, but diverse enough to demonstrate the most important physical effects and features of the method. The results involve three quantities, $\mathcal{G}_l(\tau)$, $\alpha_l(i\omega_n)$, and complex $\alpha_l(\omega)$ computed for three multipole processes: dipole−dipole ($l = 1$), quadrupole−quadrupole ($l = 2$), and octupole−octupole ($l = 3$). Each system is simulated independently with two time steps $\Delta\tau$ to probe for time-step error and to rule out the possibility of numerical artifacts. The smaller time step is used for the main results (solid line), while the bigger provides a "sanity check" (dotted line): the results are roughly as reliable as the two independent results are inseparable. The molecular simulations are repeated at various temperatures between 200 and 1600 K to probe for weak and strong thermal effects. Finally, we use $\alpha_l(i\omega_n)$ to compute dispersion coefficients between pairs of species at 300 K. For reference, Table 1 contains a compilation of all static polarizabilities and total energies, and their statistical error estimates: 2σ standard error of the mean (2SEM). Agreement

DOI: 10.1021/acs.jctc.8b00859
J. Chem. Theory Comput. XXXX, XXX, XXX−XXX

Table 1. Comparison of Total Energies and Static Polarizabilities (with 2SEM Estimates) from the PIMC Simulations and Available 0 K References[a]

	T (K)	E	$\Delta\tau$	$\alpha_1(0)$	$\alpha_2(0)$	$\alpha_3(0)$
H	2000	−0.49993(2)	0.05	4.5023(9)	15.011(7)	131.4(2)
	300	−0.5000(2)	0.02	4.50(3)	15.03(12)	132(3)
	0	−0.5		4.5[b]	15.0[b]	131.25[b]
He	2000	−2.9036(4)	0.0125	1.382(3)	2.435(9)	10.49(9)
	300	−2.904(2)	0.02	1.38(4)	2.43(6)	10.5(4)
	0	−2.90372[c]		1.383192[d]	2.445083[d]	10.620329[d]
H_2	1600	−1.15855(9)	0.05	5.519(5)	26.83(5)	125.7(7)
	800	−1.16168(12)	0.05	5.463(6)	34.38(9)	123.0(8)
	400	−1.1630(2)	0.05	5.424(10)	47.7(3)	121.4(9)
	300	−1.1633(8)	0.02	5.42(6)	53.4(10)	118(3)
	200	−1.1637(3)	0.05	5.43(3)	66.1(5)	121(2)
	0	−1.164025[e]		5.395708[f]	12.455708[f]	
	0			5.4139[g]		
HD^+	1600	−0.59047(12)	0.05	11.96(3)	152.5(5)	156.7(6)
	800	−0.59493(12)	0.05	19.04(4)	257(2)	214.9(9)
	400	−0.59663(12)	0.05	33.73(7)	468(4)	345(2)
	300	−0.5968(3)	0.02	43.6(4)	601(14)	426(8)
	200	−0.5972(2)	0.05	62.3(3)	848(10)	557(6)
	0	−0.597898[h]		395.306326[h]	2050.233354[h]	773.42727[h]
Ps_2	400	−0.51598(8)	0.05	71.57(8)	1390(20)	$5.3(4)\times10^4$
	300	−0.5158(2)	0.02	71.9(3)	1390(30)	$5.2(4)\times10^4$
	200	−0.51593(12)	0.05	71.7(2)	1370(20)	$5.1(3)\times10^4$
	0	−0.516004[i]				

[a]For H and He, the results are adiabatic, i.e., from clamped-nuclei simulations; otherwise, the results are fully nonadiabatic including rovibrational motion. All values are given in atomic units. [b]Bishop and Pipin.[50] [c]Pekeris,[51] [d]Yan et al.[52] (data truncated). [e]Pachucki and Komasa[53] (data truncated). [f]Bishop and Pipin[50] (isotropic averaging; separation $R = 1.449$; mismatch of α_2 is due to the missing rotational component). [g]Kolos and Wolniewicz[54] (isotropic averaging; separation $R = 1.4$). [h]Tang et al.[47] (data truncated). [i]Usukura and Suzuki[55] (data truncated).

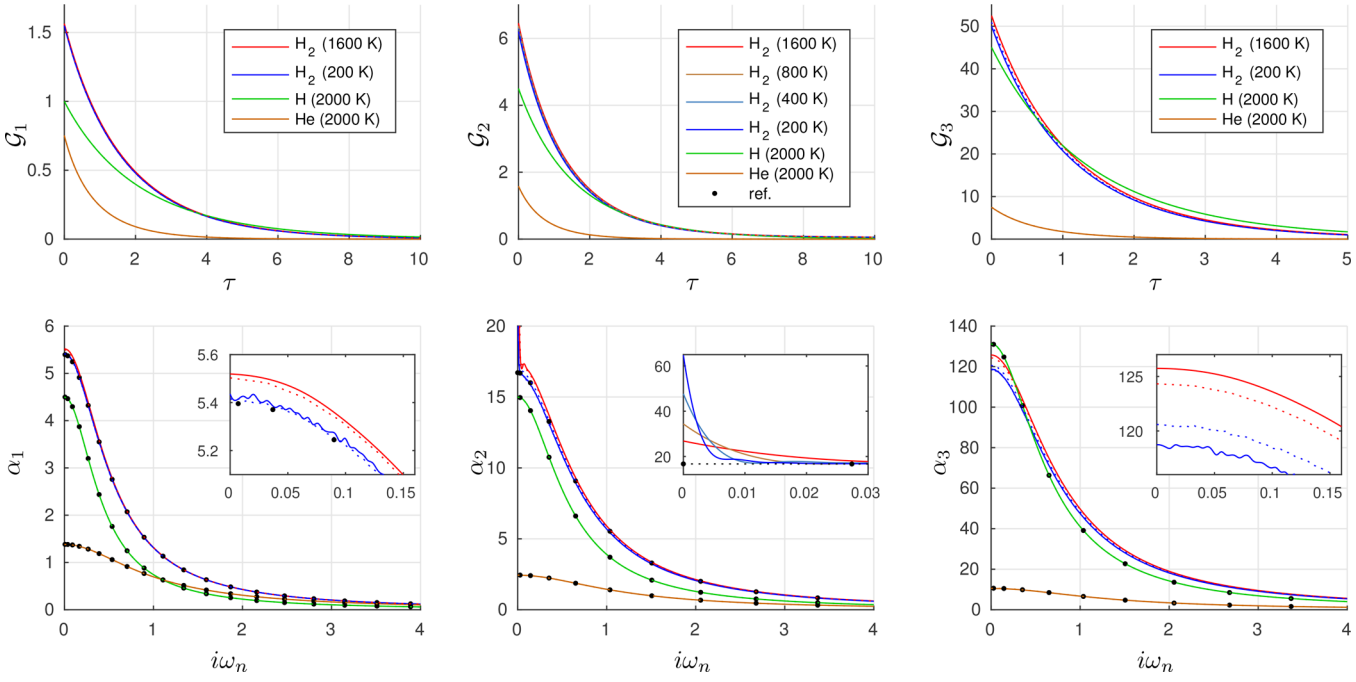

Figure 3. Correlation functions $\mathcal{G}_l(\tau)$ and Fourier transforms $\alpha_l(i\omega_n)$ of H, He, and H_2. With atoms, the thermal dependence is negligible, and the results match with 0 K reference values.[50] With H_2, there is a weak centrifugal effect that separates 200 and 1600 K results from each other and the reference in the dipole and octupole processes. On the other hand, a permanent quadrupole correlation causes a huge and thermally dependent orientational effect that is shown in the inset of α_2. It overrides the centrifugal effect and is also missing from the reference.

with the available references is excellent. All results are given in atomic units.

4.1. H and He. To establish computation of purely electronic spectra, we start with atomic species: isolated H and He. The systems are simulated in clamped-nuclei approx-

DOI: 10.1021/acs.jctc.8b00859
J. Chem. Theory Comput. XXXX, XXX, XXX−XXX

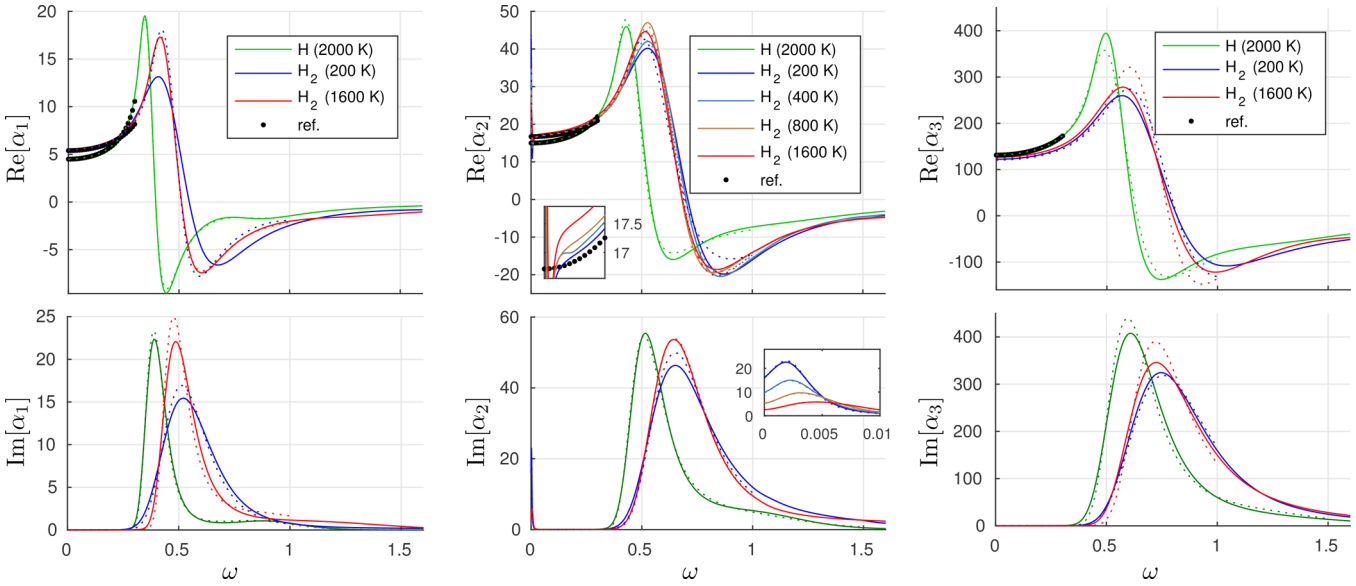

Figure 4. Dynamic polarizabilities $\alpha(\omega)$ of H and H_2. The spectral peaks of H are lower than those of H_2, but their proportions remain approximately the same in higher multipoles. While the results for H are in good agreement, H_2 shows thermal and nuclear effects that are missing from the 0 K references.[50] The quadrupole polarizability $\alpha_2(\omega)$ of H_2 has a large thermal effect due to rotational coupling: the low-frequency (IR) spectrum spreads out, and the huge orientational polarizability decreases toward higher temperatures. At higher frequencies, the difference to 0 K is explained by vibrational and centrifugal effects, and a different bond length used in ref 50. Unfortunately, different shapes of the electronic peaks are not entirely due to electron−nucleus coupling: the spectral broadening due to MaxEnt inversion is worse with the heavier, low-temperature simulations. Consequently, the results are generally sharper with the longer time step (dotted) than the shorter one (solid).

imation at T = 2000 K. At low temperatures, they are effectively in their electronic ground states. Hence, the spectra and polarizabilities are in good agreement with 0 K references.[50,64] The time steps are $\Delta\tau$ = 0.05, 0.1 for H and $\Delta\tau$ = 0.0125, 0.025 for He. The correlation functions $\mathcal{G}_l(\tau)$ and their Fourier transforms $\alpha_l(i\omega_n)$ are presented in Figure 3. Real-domain dynamic polarizabilities $\alpha_l(\omega)$ are obtained by analytic continuation and presented in Figures 4 and 5. The imaginary part $\mathrm{Im}[\alpha_l(\omega)]$ and the spectrum $A_l(\omega)$ are related, so the latter is not presented separately. The real part $\mathrm{Re}[\alpha_l(\omega)]$ provides the optical response.

Overall, agreement with the references is excellent at low frequencies, but the amount of detail is limited in the active spectral region (see Table 1 and Figures 3, 4, and 5). The same holds for all of the simulated electronic spectra. The lower moments of the MaxEnt spectrum, weight and alignment, are generally accurate. However, the higher moments providing sharpness and distinction between bound transitions are lost in the noise. Spectral weight of the continuum is relatively small for the dipole process but increases substantially with the higher multipole transitions. Our polarizabilities are slightly higher than the reference near the first electronic excitation. This mismatch results from "spilling" of the spectrum to inappropriate frequencies due to the artificial spectral broadening. The true frequency ranges between the lowest multipole transition and continuum are $0.375 < \hbar\omega < 0.5$ for H and around $0.76 < \hbar\omega < 0.90$ for He.

4.2. Ps_2. Next, we consider the nonadiabatic regime with dipositronium, Ps_2: an exotic system, whose dielectric properties, to the best of our knowledge, have not been simulated before. The positron mass equals that of electron $m_{\bar{e}} = m_e$, and the simulation is thus fully nonadiabatic. Annihilation is not considered. Ps_2 is likely to dissociate at T > 800 K,[65] so we simulate it at temperatures T = 200 and 400 K with time steps $\Delta\tau$ = 0.05 and 0.1. We have compiled the

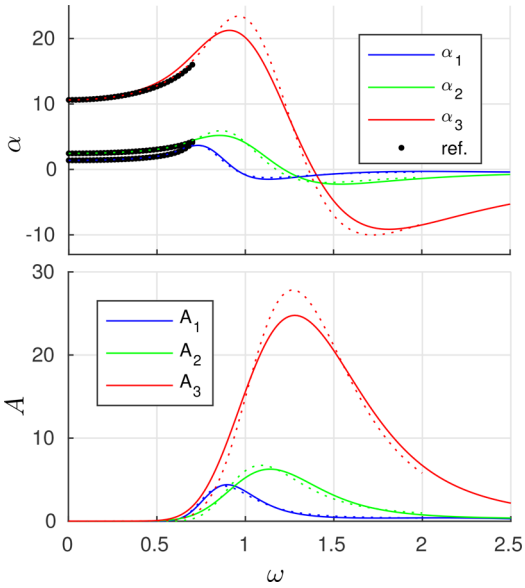

Figure 5. Real dynamic polarizabilities $\mathrm{Re}[\alpha(\omega)]$ and spectral functions $A(\omega)$ of He at 2000 K. In higher multipoles, the spectral moments grow in magnitude and frequency. The results are in good agreement between big (dotted) and small (solid) time steps and the 0 K reference.[50]

results of correlation functions and imaginary-frequency polarizability to Figure 6 and real-frequency dynamic polarizabilities to Figure 7. Total energies and static polarizabilities are found in Table 1. Pure positronic systems have much larger dielectric response than regular atoms, but otherwise they act similarly. As seen in the figures, all the imaginary-domain correlations have similar scaling and only different orders of magnitude.

DOI: 10.1021/acs.jctc.8b00859
J. Chem. Theory Comput. XXXX, XXX, XXX−XXX

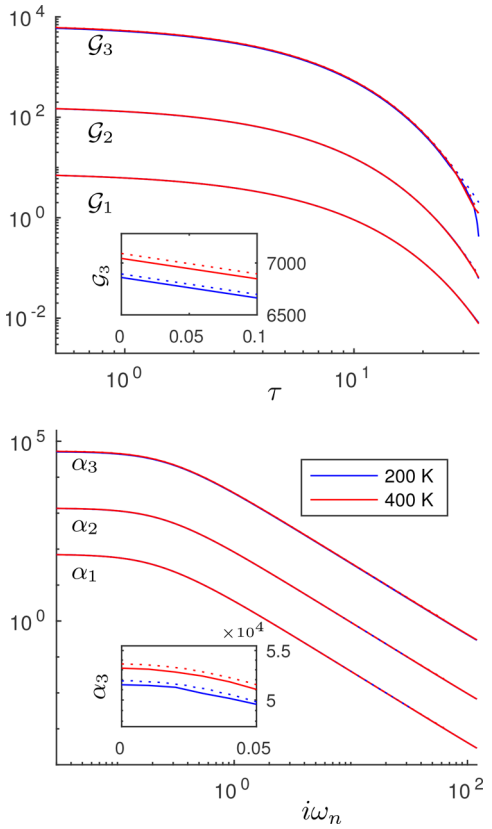

Figure 6. Logarithmic plots of $\mathcal{G}(\tau)$ and $\alpha(i\omega_n)$ of Ps_2 at 200 and 400 K. Different multipole correlations have similar scaling but different orders of magnitude. A small thermal effect increment is observed at the higher temperature. This is most pronounced in the octupole order, which is depicted in the insets.

An interesting question is the relationship between Ps_2 and Ps, the latter of which can be solved analytically. First, the bound dipole spectrum ranges of Ps ($0.1875 < \hbar\omega < 0.25$) agree with those of Ps_2 ($0.18160 < \hbar\omega < 0.24240$[55]) and the results of this work. The higher multipole spectra are shifted to higher frequencies. Second, the imaginary-time dipole correlation of Ps_2 at 300 K is approximately twice that of Ps, as shown in Figure 8. For two completely uncorrelated positroniums, this quotient would be exactly 2. The small difference is related to the binding energy of Ps_2. The quadrupole correlations cannot be compared, because α_2 is zero for Ps. The octupole processes converge to a quotient of approximately 30, but the response at low Matsubara frequencies does not show any intuitive behavior. The transient occurs at $\hbar\omega_n < 15$, which involves the first ~2500 Matsubara frequencies at 300 K.

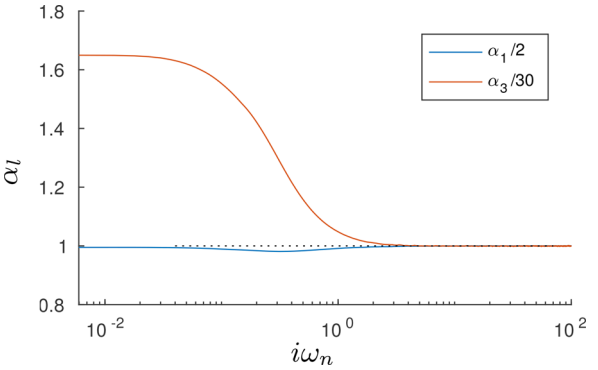

Figure 8. Scaled quotients between $\alpha_l(i\omega_n)$ of Ps_2 and Ps at 300 K. The scaling factor is chosen such that the fraction converges to unity as $i\omega_n \to \infty$. For instance, it is understandable that the dipole polarizability of Ps_2 almost equals twice that of Ps.

4.3. H_2 and HD^+. Finally, we study combined electronic, nonadiabatic, thermal, and nuclear quantum effects featured in two molecular systems: H_2 and HD^+. For both systems, the temperatures are T = 200, 400, 800, and 1600 K and time steps $\Delta\tau$ = 0.05 and 0.1. The simulation is nonadiabatic with fully quantized nuclei, using m_p = 1836.15267248m_e and m_d = 3670.480492233m_e for the respective masses of proton and deuteron. The correlation functions and imaginary-frequency polarizabilities are presented in Figures 3 and 9 depending on the multipole symmetry. Dynamic polarizabilities are shown in Figures 4 for H_2 and 10 for HD^+.

While the molecules are effectively in their electronic ground states, their nuclear motion depends on the temperature. This may cause a weak or a strong effect on the total molecular polarizability. The weak effect is related to centrifugal distortion: the bond becomes longer, if a molecule is in a high rotational ensemble (high temperature); hence, the electric moments usually get slightly larger.[42] This is most readily seen by comparing 200 and 1600 K data of $\mathcal{G}_l(\tau)$ in Figures 3 and 9.

The strong effect is caused by nonzero electric moments. The molecule pursues a favorable orientation with the

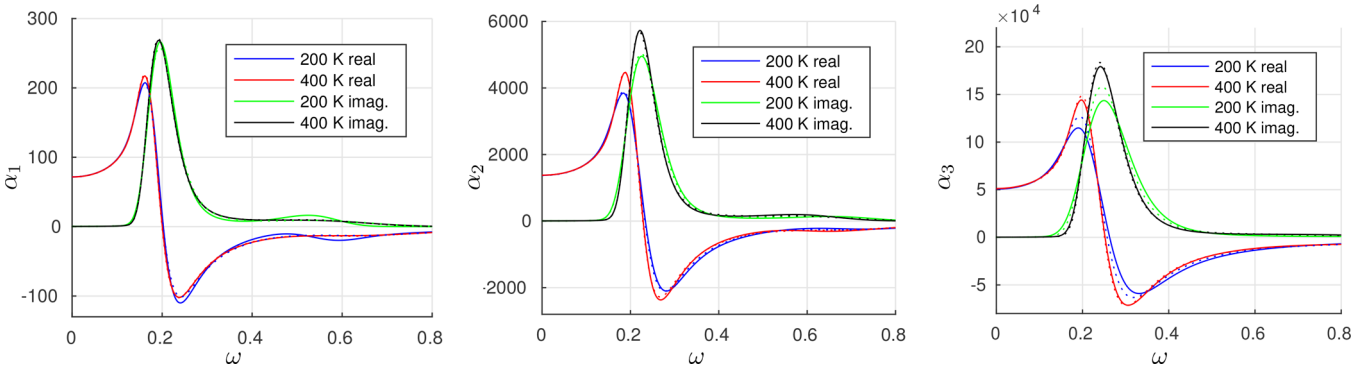

Figure 7. Dynamic polarizabilities $\alpha(\omega)$ of Ps_2 at 200 and 400 K. Here, all the spectra are located roughly at the same frequency interval, but the spectral weights escalate in higher multipoles. There is a small thermal increment in the higher multipole polarizabilities, as supported by Figure 6. The differences in spectral sharpness, however, are mostly due to the numerics.

DOI: 10.1021/acs.jctc.8b00859
J. Chem. Theory Comput. XXXX, XXX, XXX−XXX

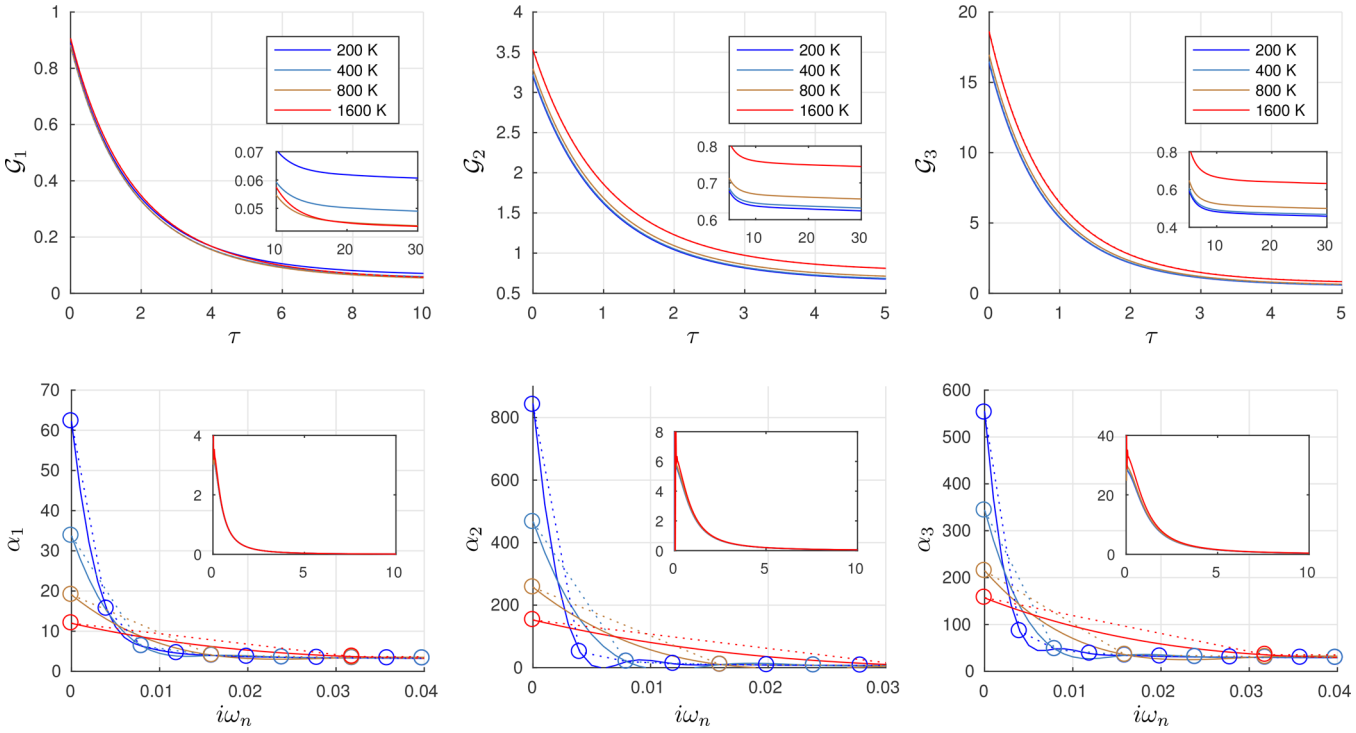

Figure 9. Correlation functions $\mathcal{G}(\tau)$ and Fourier transforms $\alpha(i\omega_n)$ of HD^+ at variable temperatures. A weak centrifugal effect is seen as $\mathcal{G}_l(\tau)$ saturates to slightly different finite values: the effect is also inverted between the dipole and the higher orders. On the other hand, $\alpha(i\omega_n)$ exhibits a strong rotational effect, which decays fast in both the temperature and the Matsubara frequencies. Thermal and time-step effects are not as complex as they first seem: rather, the error of cubic spline interpolation is demonstrated by applying it for the smaller time step (solid) but not the bigger one (dotted). The actual data points are marked with circles. The large-scale data of $\alpha(i\omega_n)$ are shown in the insets and do not have notable thermal effects at higher frequencies.

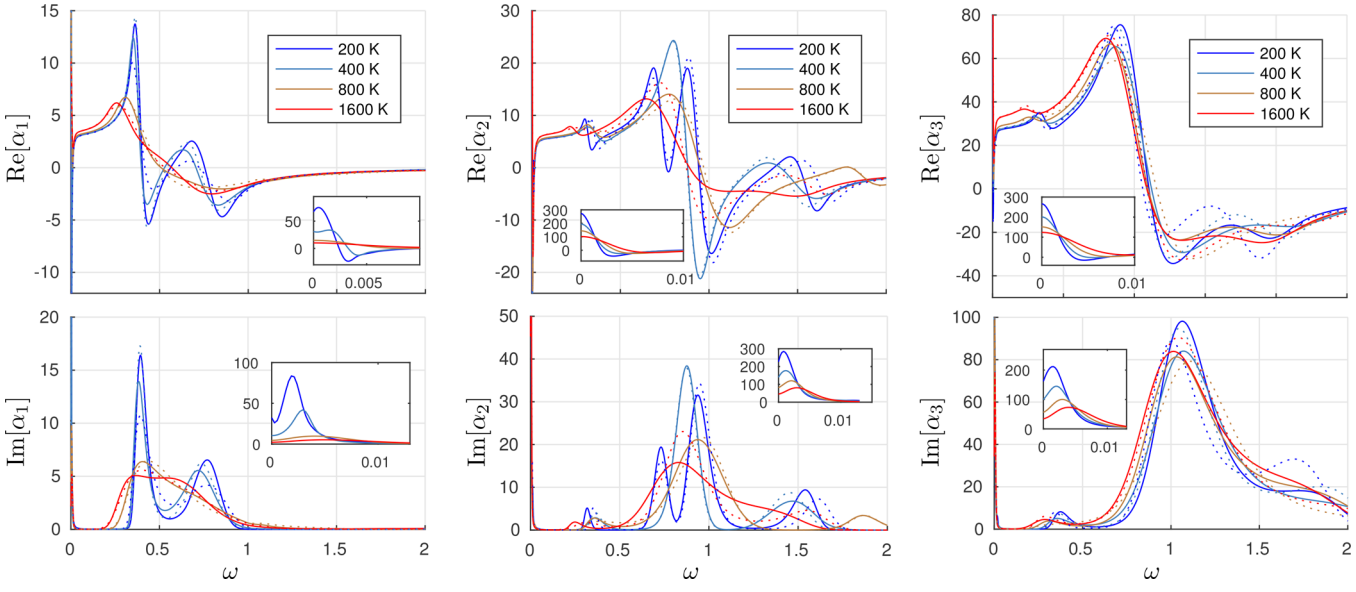

Figure 10. Dynamic polarizabilities $\alpha(\omega)$ of HD^+ at variable temperatures. HD^+ is IR-active in all multipoles, and thus, in each plot, we can see broadening of the IR spectrum and thermal decay of the orientational effect. The temperature causes considerable shifting and broadening also to the electronic spectra, only a part of which is explained by the numerical deficiency of MaxEnt. There is a reasonable agreement between the bigger (dotted) and the smaller (solid) time steps.

perturbing field, which causes a dominant, orientational contribution to the average polarizability.[41] High rotational ensemble interferes with the orientation, and hence, the rotational effect fades off as the temperature increases.[42,43,46] In higher orders, this effect is reproduced between nonzero anisotropy of tensorial polarizability and an associated hyperpolarizability.[42,43,46] Here, permanent moments are present in α_2 of H_2 and each α_l of HD^+, whose figures also have insets showing the strong decay of the rotational polarizability as T increases. At the low-temperature limit, all rotational motion is deactivated and the static polarizability saturates to a finite value.[43] Beyond the static limit, the

DOI: 10.1021/acs.jctc.8b00859
J. Chem. Theory Comput. XXXX, XXX, XXX−XXX

rotational effect fades off rapidly in terms of both real and imaginary frequencies. This limits the spectral activity of rotation to infrared frequencies. At higher frequencies, the optical properties are dictated by the electronic spectra. Therefore, our results for H_2 beyond infrared agree with isotropic averages computed with eqs 28 and 29, and the available electronic reference data.[50]

4.4. Dispersion Coefficients. Lastly, we demonstrate an additional use of imaginary-frequency polarizability data: computing London dispersion coefficients using eqs 31−33. For this purpose, we simulated H, He, H_2, HD^+, Ps, and Ps_2, the same as before but using compatible temperature and time step: T = 300 K and $\Delta\tau$ = 0.02. Proof-of-concept results between each pair of species are presented in Table 2.

Table 2. Dispersion Coefficients (with 2SEM Estimates) for Pairs of Atoms and Molecules at 300 K, Using $\Delta\tau$ = 0.02[a]

	C_6	C_8	C_{10}
H−H	6.50(4)	124.7(4)	3300(9)
	6.4990267[b,d]	124.39908[b,d]	3285.8284[b,d]
H−He	2.82(4)	41.9(3)	873(4)
	2.8213439[b,d]	41.828[b,d]	871.23[b,d]
H−H_2	8.78(7)	164.8(8)[f]	4003(12)
	8.7843286[d]	161.31542[d]	
H−HD^+	6.35(12)[f]	135(5)[f]	2620(50)[f]
	5.3815691[c]	99.592513[c]	2023.6873[c]
H−Ps	34.8(3)	318(2)	11560(60)
H−Ps_2	68.7(4)	4210(50)	$3.35(6) \times 10^5$
He−He	1.46(2)	14.09(9)	182.7(8)
	1.4609778[b,d]	14.117857[b]	183.69107[b]
He−H_2	4.01(5)	56.4(4)[f]	1008(4)
	4.0128132[d]	55.381453[d]	
He−HD^+	2.65(9)[f]	41(3)[f]	507(10)[f]
	2.3441447[c]	31.043629[c]	416.42889[c]
He−Ps	13.4(2)	60.9(6)	3040(30)
He−Ps_2	26.4(4)	1520(30)	$1.17(3)\times10^5$
H_2−H_2	12.04(12)	219.1(1.3)	4870(20)
	12.058168[d]		
H_2−HD^+	8.4(3)	184(8)	3800(200)
H_2−Ps	45.2(4)	401(4)	13270(70)
H_2−Ps_2	89.2(8)	5470(70)	$4.32(8) \times 10^5$
HD^+−HD^+	11.7(1.2)	530(70)	16000(3000)
HD^+−Ps	37(1)	510(40)	7940(120)
HD^+−Ps_2	74(3)	4800(200)	$3.7(2) \times 10^5$
Ps−Ps	207.3(1.3)	0[e]	68400(400)
Ps−Ps_2	410(3)	21000(300)	$1.59(4) \times 10^5$
Ps_2−Ps_2	811(5)	83200(800)	$1.000(12) \times 10^7$

[a]Available 0 K data provided for reference. [b]Yan et al.[52] [c]Tang et al.[47] [d]Bishop and Pipin.[50] [e]The quadrupole moment of Ps is zero by the symmetry of masses. [f]The mismatch is due to orientational and thermal effects that are missing from the reference.

Most results match the available 0 K references,[47,50,52] because as we have shown, the thermal dependency of polarizabilities is negligible for most of the systems considered here. Exceptions are the polarizabilities associated with permanent electric moments: α_2 of H_2 and all α_l of HD^+. As seen in Figures 3 and 9, they have quickly vanishing and thermally dependent rotational peaks at low Matsubara frequencies. This leads to a small yet noticeable difference between our 300 K results and the 0 K electron-only references: the peaks effectively increase the values of the dispersion coefficients; the effect of rotational coupling is attractive. Otherwise (e.g., Ps systems) the coefficients are being reported for the first time. Our approach provides a rather direct but accurate interface for incorporating nuclear quantum effects, orientational averaging, and thermal trends into weak molecular interactions.

5. SUMMARY

We have given a detailed demonstration of estimating dynamic multipole polarizabilities from all-electron PIMC simulations. In particular, we have computed autocorrelation functions of the three lowest electric multipoles and analytically continued them with the MaxEnt method. We have validated our approach by reproducing well-known reference values for some one- and two-electron systems: H, He, and H_2. However, we have also provided new complementary data, such as the higher-moment spectra and polarizabilities of H_2, HD^+, and Ps_2. Similarly, we have provided van der Waals dispersion coefficients between the aforementioned species. The coefficients are spherically averaged and include a full thermal ensemble of electric interactions at 300 K.

Indeed, the paradigm of our approach is to provide mixing, as opposed to separation, of the degrees of freedom. Of course, explicit decomposition of the electronic, rovibrational, nonadiabatic, and thermal problems can be very insightful in simple systems, such as those featured in this work. For instance, the existing models for rotational spectrum, zero-point vibration, and absorption cross-section, etc., are very intuitive and precise. Such quantum phenomena we can merely pinpoint from the PIMC results, but not quite reverse engineer. The electronic spectrum itself is a challenge to reproduce at the sharpness and precision of ab initio methods. However, for the purpose of exact mixing of all the degrees of freedom, PIMC provides a rather unique and controllable interface. This will be useful in more complex environments, where harmonic and adiabatic approximations start to fail.

The shortcomings of our approach are mostly due to the ill-posed nature of analytic continuation. A method beoynd MaxEnt is called for but, as of today, not readily available. A universal remedy is increasing computation: "to solve an ill-posed problem, nothing beats good data", as stated by Jarrell and Gubernatis.[21] After all, what counts as heavy today can well be the standard of tomorrow. In that sense, all-electron simulation with PIMC holds the future prospect of a high-accuracy electronic structure benchmark. A natural follow-up for the future will be the simulation of systems that are challenged with the exchange interaction, the fermion sign problem.

In the end, polarizability itself is rather a single example of dynamic response based on quantum correlation functions; the proposed scheme works as a template to numerous similar problems, and vice versa. A lot more will be learned and achieved by developing better practices for producing and processing QMC data, and here we have only taken a first step.

APPENDIX A: OPTIMIZING AUTOCORRELATION IN PIMC

Computation of an imaginary-time autocorrelation function can be the bottleneck of a PIMC simulation, when the number of time slices is large. It is thus reasonable to briefly discuss optimization of such a procedure.

DOI: 10.1021/acs.jctc.8b00859
J. Chem. Theory Comput. XXXX, XXX, XXX−XXX

We consider measurement of a correlation function from a sample trajectory R, which has M time slices separated by a time step $\Delta\tau$. A single measurement means choosing a reference time slice R_k and correlating it with another time slice R_{k+m} such that

$$C_{PQ}(m\Delta\tau) = P(R_k)\, Q(R_{k+m}) \tag{50}$$

where $k + m$ goes from 0 to $M - 1$ and symmetry $C_{PQ}(m\Delta\tau) = C_{PQ}(-m\Delta\tau)$ is assumed. As pointed out in eq 37, the imaginary time slices are equivalent: by shifting the reference time slice, i.e., k goes from 0 to $M-1$, we get M independent correlation functions from a single sample trajectory R. While efficient in terms of sampling, making M^2 measurements is an intensive computational task.

A few optimizations can make the practical calculation significantly faster. First, rather than measuring P or Q on the fly, an array of measurements should be stored into memory, e.g., $P_k = P(R_k)$. If the observable is tensorial, a contiguous memory layout should be preferred for the imaginary-time dimension. Second, unnecessary checkups and modification of indices should be avoided. The following pseudocode achieves this:

```
Initialize(C)
for k=0,M-1
  C(0) = C(0) + P(k)*Q(k)
  for m=k+1,M-1
    C(m-k) = C(m-k) + P(k)*Q(m) + Q(k)*P(m)
  end
end
  D(0) = C(0)/M
  for k=1,(M-1)/2  # if M is even, round up
    D(k) = ( C(k) + C(M-k-1) )/(2*M)
  end
```

where D is another array that only has $M/2$ indices. Namely, only half the data needs to be recorded because of the symmetry. Moreover, if we are computing an autocorrelation function, i.e., $Q = P$, the previous code simplifies to

```
Initialize(C)
for k=0,M-1
  for m=k,M-1
    C(m-k) = C(m-k) + P(k)*P(m)
  end
end
D(0) = C(0)/M
for k=1,(M-1)/2  # if M is even, round up
  D(k) = ( C(k) + C(M-k-1) )
end
```

The previous loops are also easy to parallelize. Third, using a finite stride is advised between the measurements and subsequent sample trajectories: e.g., only every 100th sample is measured. However, a stride in imaginary time should not be used, because it could resonate with the statistical properties of the data. Finally, using a compressed binary data format, such as the hierarchical data format (HDF), and storing the data in average bins or blocks over a large number of measurements are strongly recommended.

AUTHOR INFORMATION

Corresponding Author

*E-mail: tiihonen@iki.fi.

ORCID

Juha Tiihonen: 0000-0003-2107-911X

Ilkka Kylänpää: 0000-0002-7941-3216

Present Address

†Materials Science and Technology Division, Oak Ridge National Laboratory, Oak Ridge, TN 37831, USA.

Notes

The authors declare no competing financial interest.

ACKNOWLEDGMENTS

Juha Tiihonen has received financial support from Jenny and Antti Wihuri Foundation and Tampere University of Technology. Also, we acknowledge CSC−IT Center for Science Ltd. and Tampere Center for Scientific Computing for providing us with computational resources.

REFERENCES

(1) Berne, B. J. Path integral Monte Carlo methods: Static- and time-correlation functions. *J. Stat. Phys.* **1986**, *43*, 911−929.

(2) Ceperley, D. M. Path integrals in the theory of condensed Helium. *Rev. Mod. Phys.* **1995**, *67*, 279−355.

(3) Foulkes, W. M. C.; Mitas, L.; Needs, R. J.; Rajagopal, G. Quantum Monte Carlo simulations of solids. *Rev. Mod. Phys.* **2001**, *73*, 33−83.

(4) Cao, J.; Voth, G. A. The formulation of quantum statistical mechanics based on the Feynman path centroid density. II. Dynamical properties. *J. Chem. Phys.* **1994**, *100*, 5106−5117.

(5) Habershon, S.; Braams, B. J.; Manolopoulos, D. E. Quantum mechanical correlation functions, maximum entropy analytic continuation, and ring polymer molecular dynamics. *J. Chem. Phys.* **2007**, *127*, 174108.

(6) Weiss, S.; Egger, R. Path-integral Monte Carlo simulations for interacting few-electron quantum dots with spin-orbit coupling. *Phys. Rev. B: Condens. Matter Mater. Phys.* **2005**, *72*, 245301.

(7) Shee, J.; Zhang, S.; Reichman, D. R.; Friesner, R. A. Chemical Transformations Approaching Chemical Accuracy via Correlated Sampling in Auxiliary-Field Quantum Monte Carlo. *J. Chem. Theory Comput.* **2017**, *13*, 2667−2680.

(8) Kylänpää, I.; Räsänen, E. Path integral Monte Carlo benchmarks for two-dimensional quantum dots. *Phys. Rev. B: Condens. Matter Mater. Phys.* **2017**, *96*, 205445.

(9) Kylänpää, I.; Balachandran, J.; Ganesh, P.; Heinonen, O.; Kent, P. R. C.; Krogel, J. T. Accuracy of ab initio electron correlation and electron densities in vanadium dioxide. *Phys. Rev. Materials* **2017**, *1*, 065408.

(10) Mitroy, J.; Bubin, S.; Horiuchi, W.; Suzuki, Y.; Adamowicz, L.; Cencek, W.; Szalewicz, K.; Komasa, J.; Blume, D.; Varga, K. Theory and application of explicitly correlated Gaussians. *Rev. Mod. Phys.* **2013**, *85*, 693−749.

(11) Tubman, N. M.; Kylänpää, I.; Hammes-Schiffer, S.; Ceperley, D. M. Beyond the Born-Oppenheimer approximation with quantum Monte Carlo methods. *Phys. Rev. A: At., Mol., Opt. Phys.* **2014**, *90*, 042507.

DOI: 10.1021/acs.jctc.8b00859
J. Chem. Theory Comput. XXXX, XXX, XXX−XXX

(12) Yang, Y.; Kylänpää, I.; Tubman, N. M.; Krogel, J. T.; Hammes-Schiffer, S.; Ceperley, D. M. How large are nonadiabatic effects in atomic and diatomic systems? *J. Chem. Phys.* **2015**, *143*, 124308.
(13) Toll, J. S. Causality and the Dispersion Relation: Logical Foundations. *Phys. Rev.* **1956**, *104*, 1760−1770.
(14) Kubo, R. Statistical-Mechanical Theory of Irreversible Processes. I. General Theory and Simple Applications to Magnetic and Conduction Problems. *J. Phys. Soc. Jpn.* **1957**, *12*, 570−586.
(15) Thirumalai, D.; Berne, B. J. Time correlation functions in quantum systems. *J. Chem. Phys.* **1984**, *81*, 2512−2513.
(16) Rota, R.; Casulleras, J.; Mazzanti, F.; Boronat, J. Quantum Monte Carlo estimation of complex-time correlations for the study of the ground-state dynamic structure function. *J. Chem. Phys.* **2015**, *142*, 114114.
(17) Beach, K. S. D.; Gooding, R. J.; Marsiglio, F. Reliable Padé analytical continuation method based on a high-accuracy symbolic computation algorithm. *Phys. Rev. B: Condens. Matter Mater. Phys.* **2000**, *61*, 5147−5157.
(18) Creffield, C. E.; Klepfish, E. G.; Pike, E. R.; Sarkar, S. Spectral Weight Function for the Half-Filled Hubbard Model: A Singular Value Decomposition Approach. *Phys. Rev. Lett.* **1995**, *75*, 517−520.
(19) Mishchenko, A.; Prokof'ev, N.; Sakamoto, A.; Svistunov, B. Diagrammatic quantum Monte Carlo study of the Fröhlich polaron. *Phys. Rev. B: Condens. Matter Mater. Phys.* **2000**, *62*, 6317−6336.
(20) Nordström, J.; Schött, J.; Locht, I. L.; Di Marco, I. A GPU code for analytic continuation through a sampling method. *SoftwareX* **2016**, *5*, 178−182.
(21) Jarrell, M.; Gubernatis, J. Bayesian inference and the analytic continuation of imaginary-time quantum Monte Carlo data. *Phys. Rep.* **1996**, *269*, 133−195.
(22) Bergeron, D.; Tremblay, A.-M. S. Algorithms for optimized maximum entropy and diagnostic tools for analytic continuation. *Phys. Rev. E: Stat. Phys., Plasmas, Fluids, Relat. Interdiscip. Top.* **2016**, *94* (3), 023303.
(23) Zwanzig, R. Time-Correlation Functions and Transport Coefficients in Statistical Mechanics. *Annu. Rev. Phys. Chem.* **1965**, *16*, 67−102.
(24) Zhang, F. C.; Lee, T. K. Spectral density and magnetic susceptibility for the asymmetric degenerate Anderson model. *Phys. Rev. B: Condens. Matter Mater. Phys.* **1984**, *30*, 1556−1558.
(25) Sandvik, A. W. NMR relaxation rates for the spin-1/2 Heisenberg chain. *Phys. Rev. B: Condens. Matter Mater. Phys.* **1995**, *52*, R9831−R9834.
(26) Gallicchio, E.; Berne, B. J. On the calculation of dynamical properties of solvated electrons by maximum entropy analytic continuation of path integral Monte Carlo data. *J. Chem. Phys.* **1996**, *105*, 7064−7078.
(27) Aarts, G.; Resco, J. M. M. Transport coefficients, spectral functions and the lattice. *J. High Energy Phys.* **2002**, *2002*, 053−053.
(28) Gunnarsson, O.; Haverkort, M. W.; Sangiovanni, G. Analytical continuation of imaginary axis data for optical conductivity. *Phys. Rev. B: Condens. Matter Mater. Phys.* **2010**, *82*, 165125.
(29) Mitroy, J.; Safronova, M. S.; Clark, C. W. Theory and applications of atomic and ionic polarizabilities. *J. Phys. B: At., Mol. Opt. Phys.* **2010**, *43*, 202001.
(30) Baker, C. M. Polarizable force fields for molecular dynamics simulations of biomolecules. *Wiley Interdiscip. Rev. Comput. Mol. Sci.* **2015**, *5*, 241−254.
(31) Leontyev, I.; Stuchebrukhov, A. Accounting for electronic polarization in non-polarizable force fields. *Phys. Chem. Chem. Phys.* **2011**, *13*, 2613−2626.
(32) Liu, S.; Dykstra, C. E. Multipole polarizabilities and hyperpolarizabilities of AHn and A2Hn molecules from derivative Hartree-Fock theory. *J. Phys. Chem.* **1987**, *91*, 1749−1754.
(33) Kurtz, H. A.; Stewart, J. J. P.; Dieter, K. M. Calculation of the nonlinear optical properties of molecules. *J. Comput. Chem.* **1990**, *11*, 82−87.
(34) Dzuba, V. A.; Flambaum, V. V.; Kozlov, M. G. Combination of the many-body perturbation theory with the configuration-interaction method. *Phys. Rev. A: At., Mol., Opt. Phys.* **1996**, *54*, 3948−3959.
(35) Jamorski, C.; Casida, M. E.; Salahub, D. R. Dynamic polarizabilities and excitation spectra from a molecular implementation of time-dependent density-functional response theory: N2as a case study. *J. Chem. Phys.* **1996**, *104*, 5134−5147.
(36) Schipper, P. R. T.; Gritsenko, O. V.; van Gisbergen, S. J. A.; Baerends, E. J. Molecular calculations of excitation energies and (hyper)polarizabilities with a statistical average of orbital model exchange-correlation potentials. *J. Chem. Phys.* **2000**, *112*, 1344−1352.
(37) Chu, X.; Dalgarno, A. Linear response time-dependent density functional theory for van der Waals coefficients. *J. Chem. Phys.* **2004**, *121*, 4083.
(38) Quinet, O.; Liégeois, V.; Champagne, B. TDHF Evaluation of the dipole-quadrupole polarizability and its geometrical derivatives. *J. Chem. Theory Comput.* **2005**, *1*, 444−452.
(39) Caffarel, M.; Rérat, M.; Pouchan, C. Evaluating dynamic multipole polarizabilities and van der Waals dispersion coefficients of two-electron systems with a quantum Monte Carlo calculation: A comparison with someab initio calculations. *Phys. Rev. A: At., Mol., Opt. Phys.* **1993**, *47*, 3704−3717.
(40) Shin, D.; Ho, M.-C.; Shumway, J. Ab-initio path integral techniques for molecules. 2006, *arXiv.org ePrint archive*, arXiv:quant-ph/0611105. https://arxiv.org/abs/quant-ph/0611105.
(41) Tiihonen, J.; Kylänpää, I.; Rantala, T. T. Adiabatic and nonadiabatic static polarizabilities of H and H_2. *Phys. Rev. A: At., Mol., Opt. Phys.* **2015**, *91*, 062503.
(42) Tiihonen, J.; Kylänpää, I.; Rantala, T. T. General polarizability and hyperpolarizability estimators for the path-integral Monte Carlo method applied to small atoms, ions, and molecules at finite temperatures. *Phys. Rev. A: At., Mol., Opt. Phys.* **2016**, *94*, 032515.
(43) Tiihonen, J.; Kylänpää, I.; Rantala, T. T. Static field-gradient polarizabilities of small atoms and molecules at finite temperature. *J. Chem. Phys.* **2017**, *147*, 204101.
(44) Hohm, U.; Trümper, U. Temperature dependence of the dipole polarizability of xenon (1S0) due to dynamic non-resonant Stark effect caused by black-body radiation. *Chem. Phys.* **1994**, *189*, 443−449.
(45) Bishop, D. M.; Pipin, J. Temperature-dependence of the dynamic dipole polarizability of H2. *Mol. Phys.* **1991**, *72*, 961−964.
(46) Bishop, D. M. Molecular vibrational and rotational motion in static and dynamic electric fields. *Rev. Mod. Phys.* **1990**, *62*, 343−374.
(47) Tang, L.-Y.; Yan, Z.-C.; Shi, T.-Y.; Babb, J. F. High-precision nonadiabatic calculations of dynamic polarizabilities and hyperpolarizabilities for low-lying vibrational-rotational states of hydrogen molecular ions. *Phys. Rev. A: At., Mol., Opt. Phys.* **2014**, *90*, 012524.
(48) Bloembergen, N.; Shen, Y. R. Quantum-Theoretical Comparison of Nonlinear Susceptibilities in Parametric Media, Lasers, and Raman Lasers. *Phys. Rev.* **1964**, *133*, A37−A49.
(49) Bresme, F. Equilibrium and nonequilibrium molecular-dynamics simulations of the central force model of water. *J. Chem. Phys.* **2001**, *115*, 7564−7574.
(50) Bishop, D. M.; Pipin, J. Dipole, quadrupole, octupole, and dipoleoctupole polarizabilities at real and imaginary frequencies for H, HE, and H2 and the dispersion-energy coefficients for interactions between them. *Int. J. Quantum Chem.* **1993**, *45*, 349−361.
(51) Pekeris, C. L. Ground State of Two-Electron Atoms. *Phys. Rev.* **1958**, *112*, 1649−1658.
(52) Yan, Z.-C.; Babb, J. F.; Dalgarno, A.; Drake, G. W. F. Variational calculations of dispersion coefficients for interactions among H, He, and Li atoms. *Phys. Rev. A: At., Mol., Opt. Phys.* **1996**, *54*, 2824−2833.
(53) Pachucki, K.; Komasa, J. Schrdinger equation solved for the hydrogen molecule with unprecedented accuracy. *J. Chem. Phys.* **2016**, *144*, 164306.
(54) Kolos, W.; Wolniewicz, L. Improved Theoretical Ground-State Energy of the Hydrogen Molecule. *J. Chem. Phys.* **1968**, *49*, 404−410.

DOI: 10.1021/acs.jctc.8b00859
J. Chem. Theory Comput. XXXX, XXX, XXX−XXX

(55) Usukura, J.; Suzuki, Y. Resonances of positronium complexes. *Phys. Rev. A: At., Mol., Opt. Phys.* **2002**, *66*, 010502.
(56) Kielich, S. *Dielectric and Related Molecular Processes*, Vol. *1*; Royal Society of Chemistry: Cambridge, U.K., 1972; pp 192−387, DOI: 10.1039/9781847555878.
(57) Berne, B. J. Time-Dependent Properties of Condensed Media. In *Physical Chemisry: An Advanced Treatise. Liquid State*, Vol. *VIIIB*; Henderson, D.Elsevier, 1971; pp 539−716, DOI: 10.1016/B978-0-12-245658-9.50010-9.
(58) Stefanucci, G.; van Leeuwen, R. *Nonequilibrium Many-Body Theory of Quantum Systems: A Modern Introduction*; Cambridge University Press: Cambridge, U.K., 2013; DOI: 10.1017/CBO9781139023979.
(59) Wagnière, G. The evaluation of three-dimensional rotational averages. *J. Chem. Phys.* **1982**, *76*, 473−480.
(60) Tao, J.; Rappe, A. M. Communication: Accurate higher-order van der Waals coefficients between molecules from a model dynamic multipole polarizability. *J. Chem. Phys.* **2016**, *144*, 031102.
(61) Kylänpää, I. First-principles Finite Temperature Electronic Structure of Some Small Molecules. Ph.D. thesis, Tampere University of Technology, Tampere, Finland, 2011.
(62) Kylänpää, I.; Rantala, T. T. First-principles simulation of molecular dissociation−recombination equilibrium. *J. Chem. Phys.* **2011**, *135*, 104310.
(63) Ceperley, D. M. Path integral Monte Carlo methods for fermions. *Monte Carlo and molecular dynamics of condensed matter systems*; Euroconference on Computer Simulation Condensed Matter Physics and Chemistry; Itailian Physical Society: Bologna, Italy, 1996.
(64) Bishop, D. M.; Pipin, J. Calculation of the polarizability and hyperpolarizability tensors, at imaginary frequency, for H, He, and H2 and the dispersion polarizability coefficients for interactions between them. *J. Chem. Phys.* **1992**, *97*, 3375−3381.
(65) Kylänpää, I.; Rantala, T. T. Thermal dissociation of dipositronium: Path-integral Monte Carlo approach. *Phys. Rev. A: At., Mol., Opt. Phys.* **2009**, *80*, 024504.

DOI: 10.1021/acs.jctc.8b00859
J. Chem. Theory Comput. XXXX, XXX, XXX−XXX